ORNL/TM-2024/3519

Preliminary Results on Process Modeling Tools for Determining Variability in Additively Manufactured Stainless Steel 316 Parts

Gerry Knapp
John Coleman
Matt Rolchigo
Benjamin Stump
Alex Plotkowski

Approved for public release.
Distribution is unlimited.

August 2024

M3CR-22OR0403043

OAK RIDGE National Laboratory

ORNL/TM-2024/3519

Advanced Materials and Manufacturing Technologies Program

PRELIMINARY RESULTS ON PROCESS MODELING TOOLS FOR DETERMINING VARIABILITY IN ADDITIVELY MANUFACTURED STAINLESS STEEL 316 PARTS

Gerry Knapp
John Coleman
Matt Rolchigo
Benjamin Stump
Alex Plotkowski

August 2024

M3CR-22OR0403043

Prepared by
OAK RIDGE NATIONAL LABORATORY
Oak Ridge, TN 37831
managed by
UT-BATTELLE LLC
for the
US DEPARTMENT OF ENERGY
under contract DE-AC05-00OR22725

CONTENTS

LIST OF FIGURES

LIST OF TABLES

LIST OF ABBREVIATIONS

AM	additive manufacturing
AMMT	Advanced Materials and Manufacturing Technologies
AMMT DOE 05	"2023-04-11-AMMT_DOE_05"
AMMT DOE 06	"2023-04-18-AMMT_DOE_06"
CA	cellular automata
DOE	US Department of Energy
EBSD	electron backscatter diffraction
GCDs	Graphics Compute Dies
ISO	International Organization for Standards
L-PBF	laser powder bed fusion
MDF	Manufacturing Demonstration Facility
MPI	message passing interface
ORNL	Oak Ridge National Laboratory
RVE	representative volume element
SS316	stainless steel 316

ABSTRACT

The Advanced Materials and Manufacturing Technologies program [1] aims to accelerate the development, qualification, demonstration, and deployment of advanced materials and manufacturing technologies to enable reliable and economical nuclear energy. However, the distinct characteristics of additive manufacturing (AM) materials, stemming from their unique processing history, microstructure, and properties, pose significant challenges for the qualification and certification of nuclear components. These challenges primarily arise from component-scale variations in microstructure and properties influenced by local process conditions and geometry, which affect thermal history, melt pool dynamics, and microstructure evolution. Computational modeling tools can play a crucial role in predicting and controlling this variability. This report presents preliminary results on process modeling tools designed to predict microstructure variability in additively manufactured stainless steel 316 parts. It details the software packages and physical modeling approaches employed to simulate an AM component within an automated process modeling workflow. Initial results are demonstrated through comparisons between predicted microstructures and experimental measurements across various representative processing conditions. The report concludes by discussing the challenges inherent in process modeling of AM components and outlines a plan for future development needs.

1. INTRODUCTION

Metal additive manufacturing (AM) processes enable the creation of complex geometries and offer unique material properties that are beneficial for various applications, including in the nuclear energy sector. AM components have the potential to deliver enhanced performance and reduced lead times and strengthen domestic supply chains. Despite these benefits, the adoption of AM in nuclear energy applications faces substantial challenges primarily because of qualification and certification barriers. Unlike conventional wrought processes, in which material microstructure and properties are often assumed to be uniform throughout a component, AM materials typically exhibit heterogeneous microstructures and properties that vary by location [2, 3]. These variations arise from the localized nature of energy deposition during the fusion of powder layers, which leads to a close relationship between the heat source path and a component's geometry on the resulting distribution of microstructure and properties. Consequently, the origins of microstructure and property variation in AM components need to be better understood to predict and control the effects of variation on component performance.

Modeling and simulation tools of AM processes offer insight into the physical relationships that control microstructure and property variability in AM [4]. A recent report from the US Department of Energy (DOE) Advanced Materials and Manufacturing Technologies (AMMT) program [1] provided an assessment of process modeling tools required for this purpose and noted that a major challenge was scaling their application to component-level length- and timescales [5]. The report identified the methods best suited for scaling, which include (a) medium-fidelity process modeling codes that simulate the melt pool evolution while considering real processing data, such as the laser scan path and part geometry, and (b) grain-scale cellular automata (CA) codes that simulate the explicit, as-solidified grain structure and crystallographic texture in a representative volume element (RVE) using the temperature history from a medium-fidelity process modeling code. Additionally, the report identified the need for a digital thread [6] to assimilate data from physical operations and computational modeling tools in a unified and autonomous workflow. Ideally, this digital thread would be able to use metadata for manufactured parts (e.g., part design and performance data) as well as simulation data in a format that can be communicated to and interpreted by other tools within the digital ecosystem.

A particular area in which computational simulations can provide a tangible benefit to accelerate qualification and certification of AM parts is the prediction of local grain morphology and crystallographic texture. These microstructure features are currently impossible to measure in situ during manufacturing on commercial laser powder bed fusion (L-PBF) systems and can be expensive and time-consuming to characterize ex situ. This report presents an update on the current status of process modeling tools used to predict variability for stainless steel 316 (SS316) components processed by L-PBF AM within the the AMMT program [1]. The predicted microstructures in three RVEs located in parts produced with different process parameters are shown as preliminary results, and the predicted physical trends are described. Finally, a short discussion on future areas of modeling and simulation improvements for predicting microstructure variability in AM are provided.

2. METHODS

The software stack for modeling and simulating microstructure variation in additively manufactured parts is shown in Fig. 1, where contributions to software development by Oak Ridge National Laboratory (ORNL) are highlighted in green. The main components include the following:

- **AdditiveFOAM** (`https://github.com/ORNL/AdditiveFOAM`) is a multiphysics computational fluid dynamics code built on the OpenFOAM finite volume library. AdditiveFOAM addresses the challenge of disparate length scales between the melt pool and the simulated part through a volumetric source term in the energy equation used to approximate computationally expensive physics, adaptive mesh refinement, and the message passing interface (MPI) for parallel execution on CPUs.
- **ExaCA** (`https://github.com/LLNL/ExaCA`) is a CA code used to predict explicit representations of the grain structure in as-solidified alloys. ExaCA uses the Kokkos library [7] and (GPU-aware) MPI for performance portability on both CPUs and GPUs to simulate some of the largest (in terms of the number of cells) grain structures reported in the existing literature [8].
- **Myna** (`https://github.com/ORNL-MDF/Myna`) is a data mediation and workflow management tool for AM simulations implemented as a Python package. Myna leverages AM build data, such as process parameters and part geometry, to automatically configure and launch various types of simulations corresponding closely to as-built conditions.

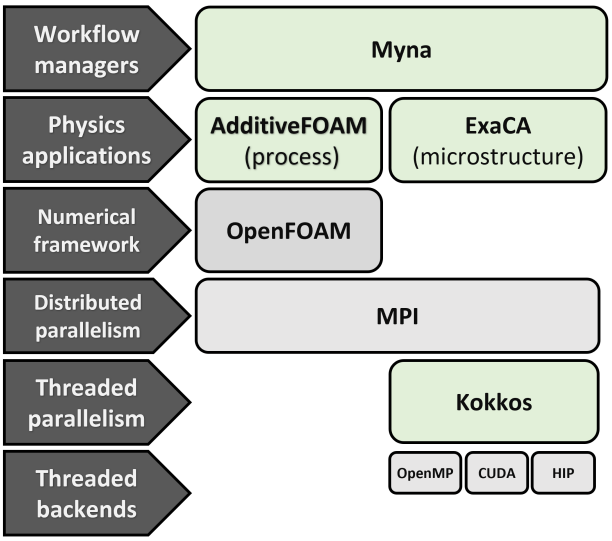

Figure 1. Software stack for AMMT process variability project. ORNL developed tools are displayed in green.

2.1 MELT POOL MODELING

Simulating AM parts starts with a process model linking the moving heat source—a laser in L-PBF—to the temperature field evolution and phase transformations in the material. In fusion-based processes, the key physical phenomena to consider are the interactions of the laser with the melt pool surface and the heat

transport in and around the melt pool. The formation of a vapor cavity and strong surface tension–driven forces at the vapor–liquid interface are known to significantly affect melt pool evolution [9], which can dramatically influence the resulting grain structure development [10]. Although high-fidelity models of the vapor–liquid interface have been applied to laser melting processes to accurately simulate these physical effects—for example, the ALE3D model of Khairallah et al. [11]—the computational cost of simulating the free surface and fluid flow in the melt pool prohibits their extension to the component scale. Instead, the effect of these high-fidelity physics are often considered effectively through the use of volumetric heat source models [12], which are applied as source terms in the energy conservation equation. AdditiveFOAM adopts this methodology while using a dynamic implementation of the heat source model, whose free parameters can be calibrated against experimental data to improve the accuracy of melt pool shape predictions over conventional static models [13].

The model begins with the definition for conservation of energy:

$$\rho c_p \left[\frac{\partial T}{\partial t} + \nabla \cdot (\mathbf{u} T) \right] = \nabla \cdot (k \nabla T) + \rho L_f \frac{\partial f_s}{\partial t} + \dot{Q}(\mathbf{x}, t), \tag{1}$$

where ρ is density, c_p is specific heat at constant pressure, $\mathbf{u}$ is velocity, T is temperature, t is time, k is thermal conductivity, L_f is latent heat of fusion, f_s is the solid mass fraction, and $\dot{Q}(\mathbf{x}, t)$ is a volumetric heating rate, which is a function of position $\mathbf{x}$ and time.

The first source term in Eq. (1) accounts for the evolution of latent heat during the solid–liquid phase change, applied as a linear temperature–solid fraction relationship across the alloy freezing range. The second source term in Eq. (1) accounts for the heat input to the system by the moving laser, which is modeled using the two-parameter, dynamic heat source model derived in Coleman et al. [13]:

$$\dot{Q}(\mathbf{x}, t) = \frac{\eta P}{V_0} \exp\left(- \left[\frac{\Delta x^2 + \Delta y^2}{r^2} \right]^{k/2} \right), \tag{2}$$

where η is the effective absorption, P is the laser power, Δx and Δy are the relative distances from the laser center, and the coefficient k is the radial distribution parameter for a super-Gaussian profile. The radial width of the volumetric heating profile is a function of depth such that:

$$r = \frac{2\sigma}{\sqrt[k]{2}} \left[1 - \left| \frac{\Delta z}{d} \right|^m \right]^{1/m}, \tag{3}$$

where 2σ is half the International Organization for Standards (ISO) definition for beam width ($D4\sigma$), Δz is the relative distance from the laser center, d is the heat source depth, and m is the volumetric shape factor that controls the final shape of heat input. Finally, the volume integral of the 3D distribution is

$$V_0 = \pi \Gamma\left(1 + \frac{2}{k}\right) \left(\frac{2\sigma}{\sqrt[k]{2}} \right)^2 d \left[\frac{\Gamma\left(1 + \frac{1}{m}\right) \Gamma\left(1 + \frac{2}{m}\right)}{\Gamma\left(1 + \frac{3}{m}\right)} \right], \tag{4}$$

where $\Gamma(x)$ is the gamma function, which can be numerically computed following DiDonato et al. [14]. A schematic of the two-parameter heat source model is shown in Fig. 2 for different values of the distribution parameter k and volumetric shape parameter m.

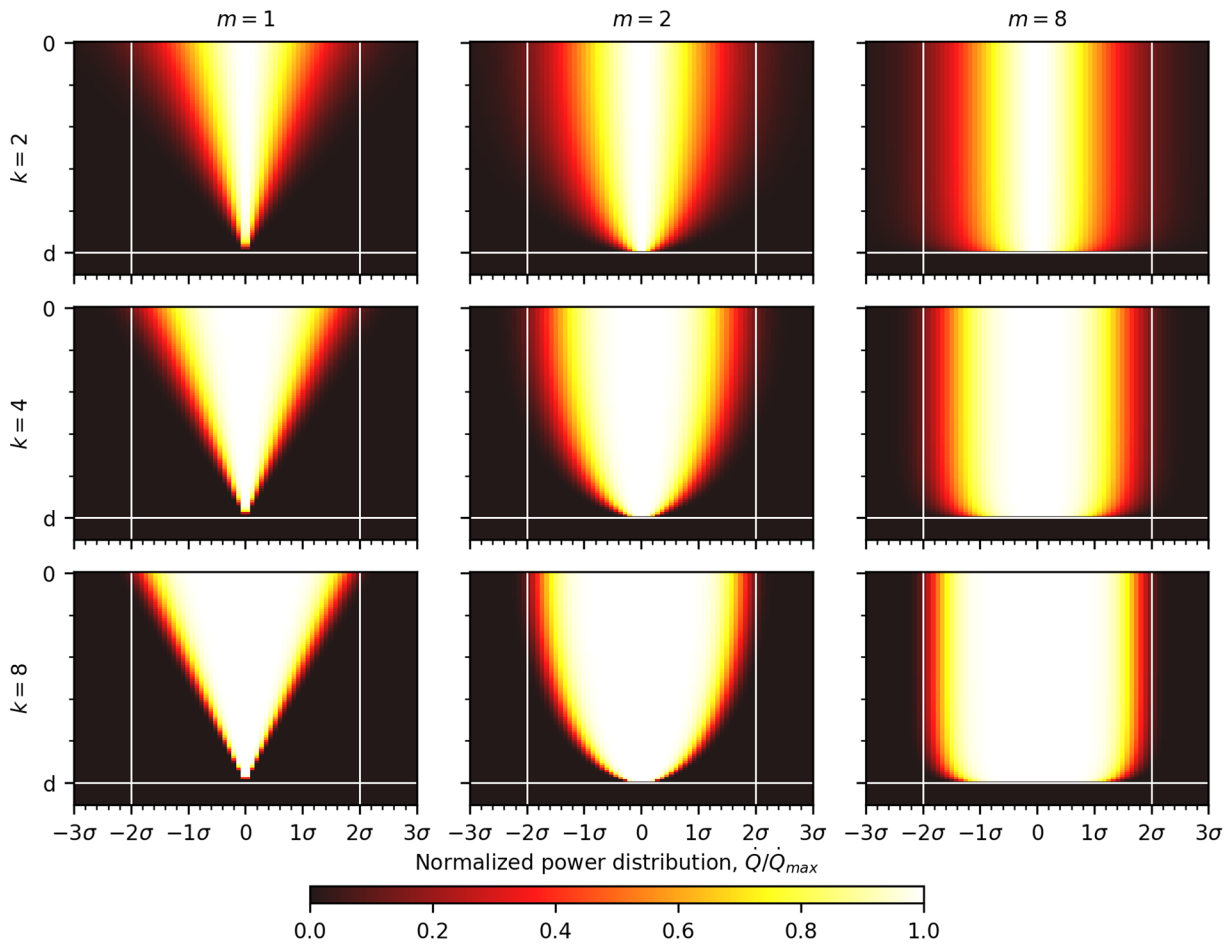

Figure 2. Representative energy input field predicted by the two-parameter heat source model for $2\sigma_x, 2\sigma_y = \sqrt{2/\pi}$, and $d = 1$. The horizontal white line shows the heat source depth d, and the vertical white lines show the heat source diameter $D4\sigma$.

This volumetric source term accounts for the effects of changing melt pool shape on transient absorption of the laser energy using the geometric expression for a conical cavity:

$$\eta(a) = \eta_0 \frac{1 + (1 - \eta_0)(G - F)}{1 - (1 - \eta_0)(1 - G)}, \tag{5}$$

where η_0 is the Fresnel absorption of the liquid metal, $G = 1/(1 + \sqrt{1 + a^2})$ is the ratio between the area of the cavity opening to the surface area of the cavity, $F = \sin^2(\theta)$ is the view factor, and $a = d/(2\sigma)$ is the aspect ratio of the cavity. The depth of the liquidus isotherm is used to calculate both the transient heat source depth in Eq. (3) and the dynamic absorption in Eq. (5). A table of the thermophysical parameters and the calibrated heat source model parameters used for SS316 are provided in Table 1.

Table 1. Thermophysical properties and modeling parameters used in simulations of SS316

Property	Value	Unit
Density, ρ	7,955	kg/m^3
Specific heat capacity (solid), $c_{p,s}$	770.4	J/(kg·K)
Specific heat capacity (liquid), $c_{p,l}$	770.4	J/(kg·K)
Thermal conductivity (solid), k_s	$4.957 + 0.01571T$	J/(m·s·K)
Thermal conductivity (liquid), k_l	$11.51 + 0.003279T$	J/(m·s·K)
Latent heat of fusion, L_f	2.68×10^5	J/kg
Liquidus temperature, T_L	1,730	K
Solidus temperature, T_E	1,670	K
Emissivity, ε	0.4	—
Fresnel absorption (liquid), η_0	0.3	—
Effective absorption, η_{eff}	0.35	—
Distribution parameter, k	7.95	—
Volumetric shape parameter, m	2.74	—

2.2 MICROSTRUCTURE MODELING

The grain structure in additively manufactured parts is complex and multiscale, including features such as dislocations at the atomistic scale, solute microsegregation and morphologies such as cells and dendrites at the micrometer length scale, and grain structures spanning the micrometer to even the millimeter length scale. To model microstructure and microstructure heterogeneity at the scale of real parts, the CA approach was used to bridge the part scale and the (sub)micrometer phenomena governing solidification of grains. Using physics-informed cell state and transition rules, CA approaches balance computationally tractability and accuracy and have been applied to predict the grain size, shape, and crystallographic texture distribution observed in electron backscatter diffraction (EBSD) data from additively manufactured parts [15, 16, 17, 18, 19, 20].

For modeling process–microstructure relationships as part of the AMMT project, the CA-based ExaCA software is being used. Developed as part of the ExaAM initiative within the Exascale Computing Project, ExaCA has the capability to leverage GPUs on supercomputers such as Summit and Frontier to perform large-scale ensembles of explicit grain structure prediction [21]. ExaCA microstructure predictions as part of the AMMT workflow are driven by time–temperature history data produced by AdditiveFOAM heat transport simulations through an input file format described in Rolchigo et al. [22]. The local undercooling of a CA cell containing the solid–liquid interface, ΔT, is linked to the ExaCA interface advance velocity via an interfacial response function, $V(\Delta T)$, which in turn bridges the scales between the modeled solidification of the grain and the approximate solute segregation, diffusion, and dendrite tip kinetics. The most common interfacial response function forms used to model austenitic stainless steel are a power law,

$$V(\Delta T) = A(\Delta T)^B; \tag{6}$$

and a cubic polynomial,

$$V(\Delta T) = \frac{\Delta t}{\Delta x} \cdot (A(\Delta T)^3 + B(\Delta T)^2 + C(\Delta T) + D), \tag{7}$$

with various examples of each present in the CA modeling literature [23, 24, 25, 26]. To approximate the stainless steel SS316, this project is currently using Equation 6 with $A = 7.325 \times 10^{-6}$ and $B = 3.12$ from Tan and Li [24]. Other CA model inputs used for AMMT program project simulations are given in 2. As part of future work, unique forms of $V(\Delta T)$ will be reevaluated for SS316L and SS316H, with unique functions for the ferrite and austenite phases.

ExaCA simulates the addition of new cells to existing grains by approximating the solid–liquid interface as a series of overlapping octahedral grain envelopes, in which the $\langle 1\,0\,0 \rangle$ crystallographic directions are represented by the center-to-vertex directions of a given envelope [27]. As the center-to-vertex lengths are incremented using Eqs. 6 or 7 and the local undercooling to approximate dendritic solidification, a series of simple, geometry-based rules enable mesh anisotropy-reduced computation of the crystallographic orientation-dependent competition between solidifying grains. Additionally, ExaCA simulates the nucleation of new grains in the undercooled liquid ahead of the existing grains using a nucleation density, N_0, to approximate the heterogeneity in the undercooled liquid. The undercooling needed to trigger a given nucleation event is assigned from a Gaussian distribution described by

$$f(\Delta T) = \frac{N_0}{\Delta T_\sigma \sqrt{2\pi}} exp\left(-\frac{1}{2}\left(\frac{\Delta T_N - \Delta T}{\Delta T_\sigma}\right)^2\right), \tag{8}$$

where ΔT_N is the mean nucleation undercooling, and ΔT_σ is the standard deviation of the distribution.

Figure 3 shows previous ExaCA simulation results that have produced grain structure predictions on the order of cubic millimeters, comparing favorably with EBSD data from the thin and thick leg supports from the AMBench-2018-01 test artifact. Calibration of ExaCA's nucleation parameters has been performed previously as part of the ExaAM challenge problem simulations; however, as shown in Figure 4, calibrating to grain area using nucleation parameters alone will yield an underconstrained optimization problem for a fixed $V\Delta(T)$. Improving this calibration procedure by either including additional outputs (such as texture metrics) or considering additional cross sections will be a necessary step toward using ExaCA to accurately predict grain size for AMMT program applications. Further refinement to the nucleation algorithm, such as consideration of a nonuniform distribution of nucleation sites across the melt pool or crystallographic orientation considerations during the nucleation process, may also be necessary for improved model accuracy.

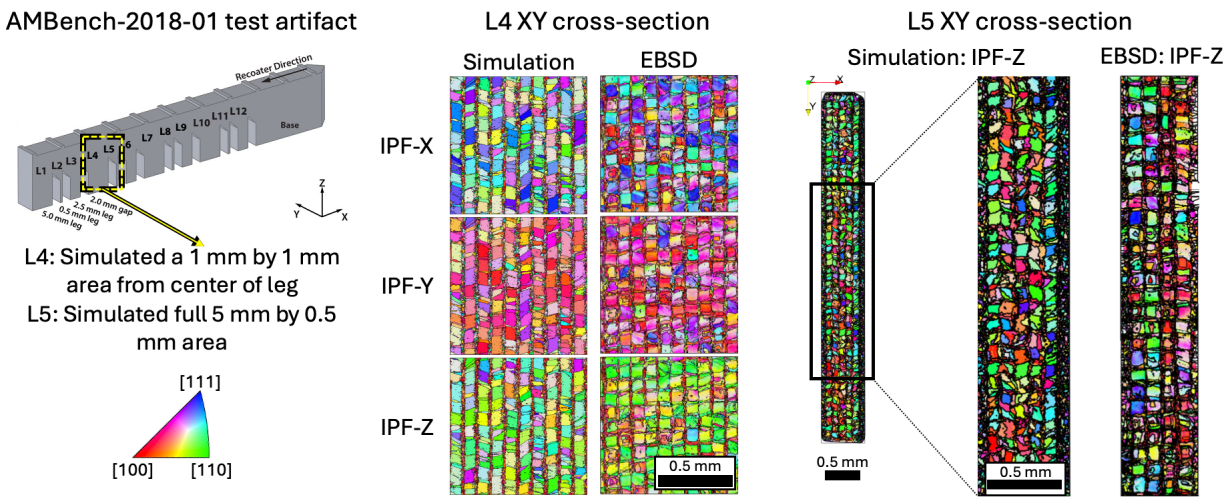

Figure 3. ExaCA grain structure predictions using representative thermal data for the L4 leg interior and the L5 leg of the AMBench-2018-01 test artifact [8, 10], alongside analogous EBSD data from Stoudt et al. [28].

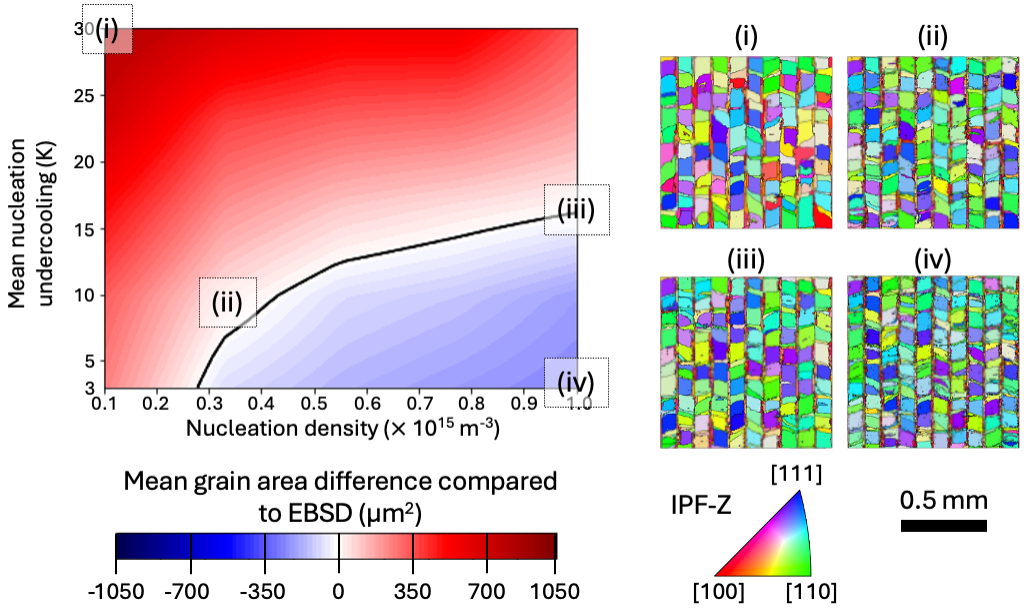

Figure 4. ExaCA mean grain area predictions produced as part of the ExaAM challenge problem simulations of the AMBench-2018-01 L4 leg. Mean grain area predictions are plotted in nucleation input parameter space as relative values compared with the EBSD data from Stoudt et al. [28]. Also shown are four representative *XY* cross sections from which mean grain areas were extracted and colored using the inverse pole figure map.

Table 2. ExaCA model input parameters for SS316

Parameters	Symbols	Values	Units
Cell size	Δx	2.5	μm
Time step	Δt	0.125	μs
Layer height	H	50	μm
Average substrate grain size	S_0	12.3	μm
IRF coefficient	A	7.325×10^{-6}	$m/K \cdot s$
IRF power	B	3.12	—
Heterogeneous nucleation density	N_0	2.5×10^{14}	m^{-3}
Mean nucleation undercooling	ΔT_N	21	K

2.3 SIMULATION USING THE DIGITAL THREAD

Research at the ORNL Manufacturing Demonstration Facility (MDF) has been developing the infrastructure needed to demonstrate a digital factory concept that tracks data from various manufacturing operations [29]. These data include in situ data from the manufacturing process, changes in sample geometry from machining, and data from characterization operations. Peregrine [30] has been created specifically for L-PBF to extract and process this in situ and characterization data to identify build anomalies [31]. The structured data from each build provide a rich, machine-readable context.

Modeling and simulation work has begun to leverage the aforementioned digital factory resources at the MDF to configure and run simulations, followed by registering the simulation data back to other build data. Initial work used the scan path and laser configuration data stored by Peregrine to initialize corresponding semianalytical heat transfer simulations that, combined with a machine learning clustering algorithm, identified regions with dissimilar solidification conditions [32]. The general workflow of configuring a simulation based on a database of relevant process data, launching the configured simulation, and finally postprocessing and analyzing the results has been developed into a software package called Myna under the MDF program.

The coupling of melt pool heat transfer simulations in AdditiveFOAM and solidification microstructure simulations in ExaCA has been incorporated in Myna and leveraged for simulation builds manufactured for the AMMT program. Using scan paths extracted from the L-PBF system, along with laser spot size, material information, part geometry, layer thickness, and coordinates for a region of interest, Myna updates AdditiveFOAM cases for each layer to be simulated. The completed AdditiveFOAM simulations are used as input data for a corresponding ExaCA simulation, which is also configured by Myna using the same build data. This workflow is shown in Figure 5, which highlights the class-based implementation of simulation types within the Myna framework and describes the requirements for the steps to simulate the as-built solidification microstructure.

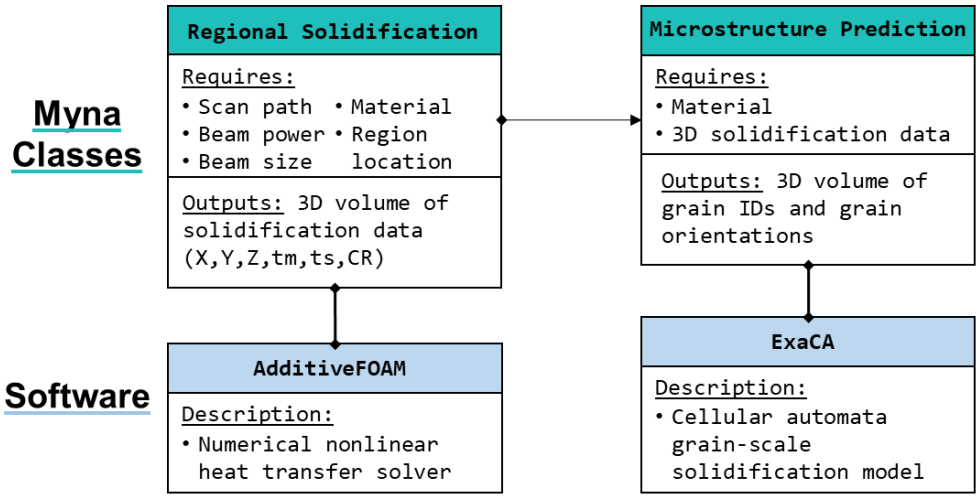

Figure 5. Schematic of the Myna class-based simulation workflow steps used for solidification microstructure simulation and the corresponding simulation software for each step.

3. PRELIMINARY RESULTS

Using the Myna framework supported by AdditiveFOAM and ExaCA, solidification microstructures were predicted for several regions of interest within AM builds manufactured for the AMMT program at the MDF. Two design-of-experiment builds on the Concept M2 L-PBF system were chosen for demonstrating the modeling capabilities: "2023-04-11-AMMT_DOE_05" (AMMT DOE 05) and "2023-04-18-AMMT_DOE_06" (AMMT DOE 06). These builds consisted of sample coupons with a cylindrical bulk region in the lower layers of the part and smaller fin-like features at the top layers of the part. Parts were manufactured with different process parameters to explore design space, and a selection of parts with preliminary microstructure predictions are summarized in Table 3.

Table 3. Summary of processing parameters used for SS316 parametric study

Build Name	**Sample**	**Power (W)**	**Speed (m s^{-1})**	**Spot Size ($D4\sigma$, μ m)**	**Linear Energy Density (J m^{-1})**
AMMT_DOE_05	P7	380	0.75	125	506
AMMT_DOE_05	P35	200	0.78	125	256
AMMT_DOE_06	P24	290	1.5	125	193

Figure 6 shows the location of several regions of interest within the part geometries. At each location, an RVE was simulated to avoid the computational barriers associated with simulating the entire part. Figure 6(a) shows the locations within the AMMT DOE 05 build, with the RVEs located in the bulk region of the part (RVE0 and RVE1). Figure 6(b) shows the locations within the AMMT DOE 06 build, which contains additional RVEs in the fin regions (RVE2 and RVE3). Myna extracted the necessary build data that had been stored by Peregrine on the digital factory platform, and the corresponding AdditiveFOAM and ExaCA simulations were configured and executed. Figure 6(c) shows the solidification start time data associated with the AdditiveFOAM-simulated melt pools, which was provided to ExaCA along with the associated melting times and cooling rates during solidification (see ref. [33] for details). ExaCA then used this time–temperature history data to simulate grain morphology and crystallographic texture, as shown in Figure 6(d).

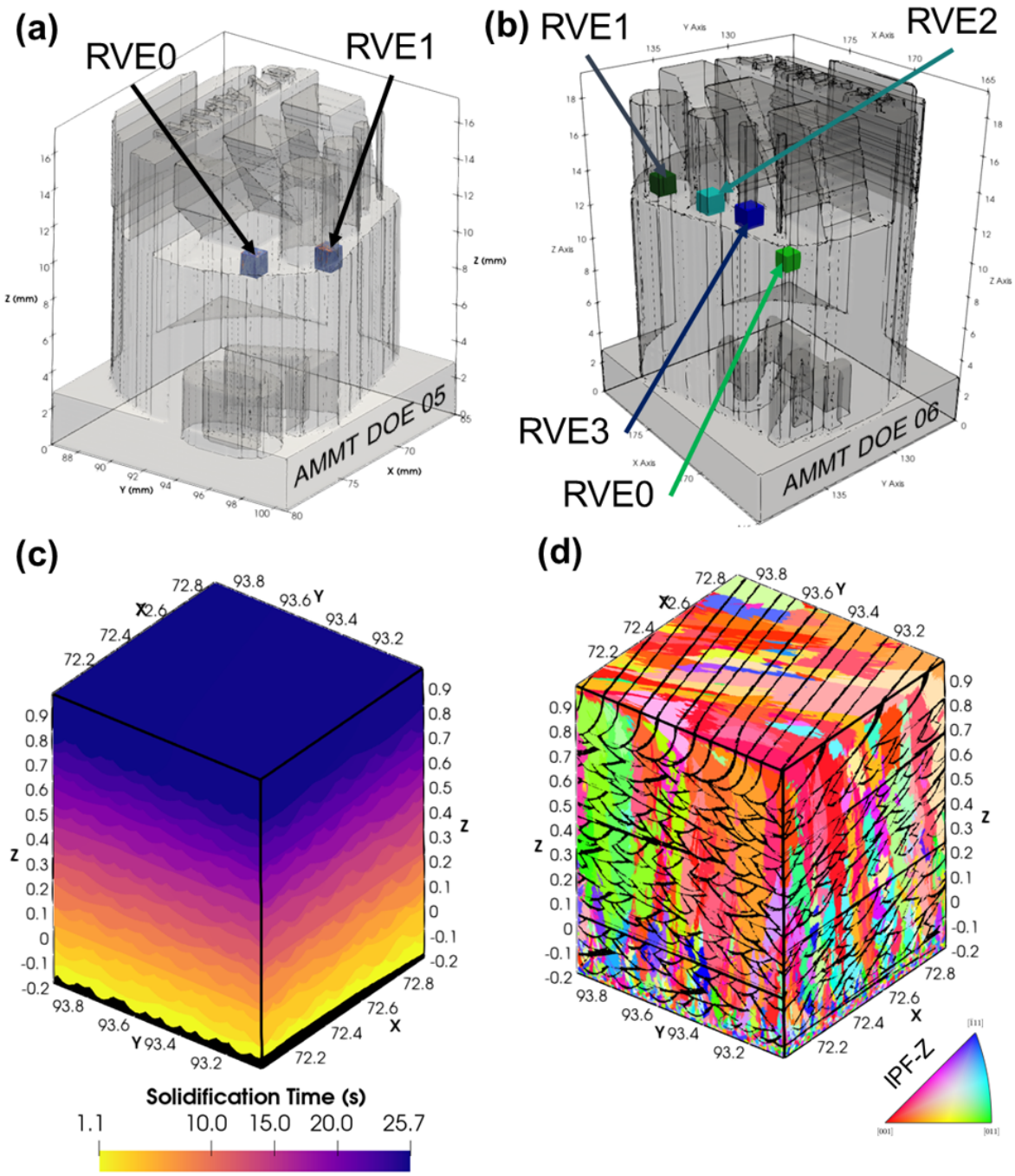

Figure 6. (a) RVE locations for samples in the AMMT DOE 05 build and (b) RVE locations in the AMMT DOE 06 build. (c) Example AdditiveFOAM solidification data for the AMMT DOE 05 P7 RVE0 location, and (d) the corresponding ExaCA prediction of the solidification microstructure.

The total wall-clock time to simulate each RVE was about 2 h on a single node of the ORNL Frontier supercomputer, consisting of one 64-core AMD EPYC-3 CPU and four AMD MI250X GPUs, each with two Graphics Compute Dies (GCDs), for a total of eight GCDs per node. AdditiveFOAM meshing and simulation took approximately 1–1.25 h/RVE where the finest mesh elements were 10 μm. ExaCA simulation took approximately 0.75–1 h/RVE with a cell size of 2.5 μm, which was chosen to limit the wall-clock time to below 2 h. Work is ongoing to validate the selection of an appropriately converged CA cell size for AM conditions.

Figure 7 shows 2D cross sections of the predicted microstructures for three RVEs located in parts produced with different process parameters, as indicated in 3. AMMT DOE 05 P7 had the highest linear energy density (power divided by velocity), and Figure 7(a) shows that the simulated microstructure consists of large columnar grains with $\langle 1\,0\,0 \rangle$ and similar crystallographic directions preferentially aligned with the build direction (i.e., more red, orange, and yellow coloring is present). AMMT DOE 05 P35 had an intermediate linear energy density, and Figure 7(b) shows that the simulated microstructure contains some lack of fusion regions where the melt pools did not fully overlap between tracks, which are annotated with black arrows. AMMT DOE 06 P24 had the lowest linear energy density, and Figure 7(c) shows that the simulated microstructure contains a significant lack of fusion because the melt pool depths were shallower than the layer thickness.

Although AMMT DOE 05 P35 and AMMT DOE 06 P24 may actually contain lack of fusion porosity in the physical specimens, its effect on the simulated microstructure is clearly nonphysical. In regions where the thermal data do not overlap between passes or layers, the existing CA rules lack the logic to nucleate or grow grains through the corresponding unmelted regions of the powder layer. Consequently, the simulated microstructure contains epitaxial grains that tend to be interrupted in a nonphysical manner. This issue is further compounded by the assumptions of a flat melt pool top surface and fixed layer spacing, leading to grains that are often interrupted along horizontal lines. To enhance the fidelity of these simulations, future research must refine the models to better account for the consolidation of powder particles and the curvature of free surfaces, which result in nonuniform layer heights in both the melt pool model (AdditiveFOAM) and the microstructure model (ExaCA).

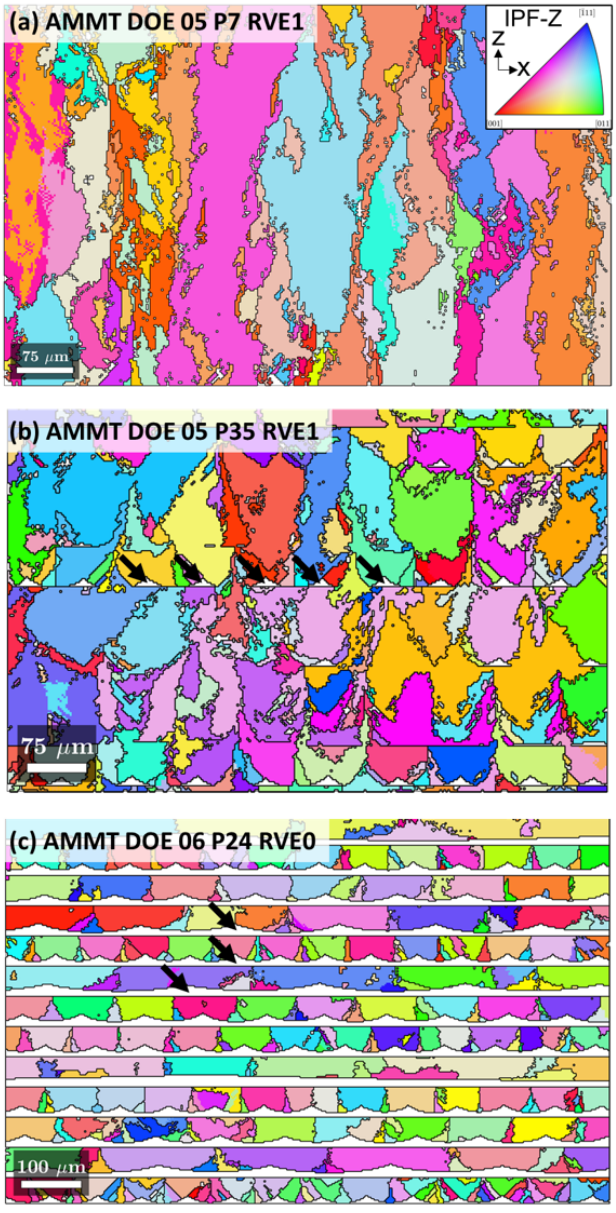

Figure 7. Microstructure from select regions within the part, as specified in Figure 6. (a–c) correspond to the regions labels in the figures, showing an *XZ* slice through the center of the simulated volumes, colored by the grains' crystallographic orientations using an inverse pole figure color map.

4. CONCLUSIONS

This report summarizes the current status of process modeling tools used to predict variability for SS316 components processed by L-PBF AM within the AMMT program [1]. Currently, the simulations for the melt pool dynamics (AdditiveFOAM) and microstructure evolution (ExaCA) have been applied within a digital thread through the development of the Myna framework. The predicted microstructures in three RVEs located in parts produced with different process parameters are shown as preliminary results. The predicted microstructures reveal a densification of the part through the removal of lack of fusion defects as the linear energy density is increased. In the fully dense part, the microstructure consists of columnar grains that grow epitaxially along the build direction with $\langle 1\,0\,0 \rangle$ and similar crystallographic directions. Future work will focus on comparing these microstructure predictions against experimental observations to assess model accuracy and identify potential paths for modeling and simulation improvements.

5. ACKNOWLEDGEMENTS

This research was made possible by the US Department of Energy, Office of Nuclear Energy, under the Advanced Materials and Manufacturing Technologies Program. We would like to thank Chase Joslin for his contributions in fabricating the AM builds and registering their data into Peregrine for use in the digital thread. We would also like to thank Luke Scime, William Halsey, and Zack Snow for their work in developing capabilities in Peregrine to process and output data for use in the digital thread.

6. REFERENCES

[1] Meimei Li et al. *Department of Energy Office of Nuclear Energy Advanced Materials and Manufacturing Technologies (AMMT) 2022 Roadmap*. Report ANL-23/12. 2022.

[2] Narendran Raghavan et al. "Influence of geometry on columnar to equiaxed transition during electron beam powder bed fusion of IN718". In: *Additive Manufacturing* 47 (2021), p. 102209.

[3] A. A. Antonysamy, J. Meyer, and P. B. Prangnell. "Effect of build geometry on the β-grain structure and texture in additive manufacture of Ti6Al4V by selective electron beam melting". In: *Materials Characterization* 84 (2013), pp. 153–168. ISSN: 1044-5803. DOI: https://doi.org/10.1016/j.matchar.2013.07.012. URL: https://www.sciencedirect.com/science/article/pii/S1044580313002131.

[4] H. L. Wei et al. "Mechanistic models for additive manufacturing of metallic components". In: *Progress in Materials Science* 116 (2021), p. 100703. ISSN: 0079-6425. DOI: https://doi.org/10.1016/j.pmatsci.2020.100703. URL: https://www.sciencedirect.com/science/article/pii/S0079642520300670.

[5] Alex Plotkowski et al. "Assessment of Process Modeling Tools for Determining Variability in Additively Manufactured Parts". In: (Mar. 2023). DOI: 10.2172/1989564. URL: https://www.osti.gov/biblio/1989564.

[6] Deborah Mies, Will Marsden, and Stephen Warde. "Overview of Additive Manufacturing Informatics: "A Digital Thread"". In: *Integrating Materials and Manufacturing Innovation* 5.1 (2016), pp. 114–142. ISSN: 2193-9772. DOI: 10.1186/s40192-016-0050-7. URL: https://doi.org/10.1186/s40192-016-0050-7.

[7] Christian R. Trott et al. "Kokkos 3: Programming Model Extensions for the Exascale Era". In: *IEEE Transactions on Parallel and Distributed Systems* 33.4 (2022), pp. 805–817. DOI: 10.1109/TPDS.2021.3097283.

[8] Matt Rolchigo et al. "ExaCA: A performance portable exascale cellular automata application for alloy solidification modeling". In: *Computational Materials Science* 214 (2022), p. 111692. ISSN: 0927-0256. DOI: https://doi.org/10.1016/j.commatsci.2022.111692. URL: https://www.sciencedirect.com/science/article/pii/S0927025622004189.

[9] Jordan S. Weaver, Jarred C. Heigel, and Brandon M. Lane. "Laser spot size and scaling laws for laser beam additive manufacturing". In: *Journal of Manufacturing Processes* 73 (2022), pp. 26–39. DOI: https://doi.org/10.1016/j.jmapro.2021.10.053. URL: https://www.sciencedirect.com/science/article/pii/S1526612521007854.

[10] Matt Rolchigo et al. "Grain structure and texture selection regimes in metal powder bed fusion". In: *Additive Manufacturing* 81 (2024), p. 104024. ISSN: 2214-8604. DOI: 10.1016/j.addma.2024.104024.

[11] Saad A. Khairallah et al. "High fidelity model of directed energy deposition: Laser-powder-melt pool interaction and effect of laser beam profile on solidification microstructure". In: *Additive Manufacturing* 73 (2023), p. 103684. DOI: 10.1016/j.addma.2023.103684.

[12] Ernandes J. G. Nascimento, Elisan dos Santos Magalhães, and Luiz Eduardo dos Santos Paes. "A literature review in heat source thermal modeling applied to welding and similar processes". In: *The International Journal of Advanced Manufacturing Technology* 126.7 (2023), pp. 2917–2957. ISSN: 1433-3015. DOI: 10.1007/s00170-023-11253-z. URL: https://doi.org/10.1007/s00170-023-11253-z.

[13] J. Coleman et al. "A Dynamic Heat Source Model for Laser Additive Manufacturing". In: *In preparation* XX (2024), p. XX. DOI: XXX.

[14] Armido R DiDonato and Alfred H Morris. “Computation of the incomplete gamma function ratios and their inverse”. In: *ACM Trans. Math. Softw.* 12.4 (1986), pp. 377–393. ISSN: 0098-3500. DOI: 10.1145/22721.23109. URL: https://doi.org/10.1145/22721.23109.

[15] O. Zinovieva et al. “Elastic properties of additively manufactured steel produced with different scan strategies”. In: *International Journal of Mechanical Sciences* 244 (2023), p. 108089. DOI: https://doi.org/10.1016/j.ijmecsci.2022.108089. URL: https://doi.org/10.1016/j.ijmecsci.2022.108089.

[16] Johannes Koepf et al. “Alternative Approach to Modeling of Nucleation and Remelting in Powder Bed Fusion Additive Manufacturing”. In: *Advanced Engineering Materials* 25 (May 2023), p. 2201682. DOI: 10.1002/adem.202201682.

[17] Qingge Xie et al. “An extended version of cellular automata model for powder bed fusion to unravel the dependence of microstructure on printing areas for Inconel 625”. In: *Additive Manufacturing* 73 (2023), p. 103676. DOI: 10.1016/j.addma.2023.103676.

[18] Yukai Chen et al. “Effects of process parameters on the microstructure of Inconel 718 during powder bed fusion based on cellular automata approach”. In: *Virtual and Physical Prototyping* 18.1 (2023), e2251032. DOI: 10.1080/17452759.2023.2251032. URL: https://doi.org/10.1080/17452759.2023.2251032.

[19] Kirubel Teferra and David J. Rowenhorst. “Optimizing the cellular automata finite element model for additive manufacturing to simulate large microstructures”. In: *Acta Materialia* 213 (2021), p. 116930. DOI: 10.1016/j.actamat.2021.116930.

[20] Mohammad Sadegh Mohebbi and Vasily Ploshikhin. “Implementation of nucleation in cellular automaton simulation of microstructural evolution during additive manufacturing of Al alloys”. In: *Additive Manufacturing* 36 (2020), p. 101726. DOI: 10.1016/j.addma.2020.101726.

[21] Matt Rolchigo et al. *LLNL/ExaCA: Version 2.0*. United States. DOI: https://doi.org/10.5281/zenodo.12744177. URL: https://zenodo.org/records/12744177.

[22] Matthew Rolchigo et al. “Sparse thermal data for cellular automata modeling of grain structure in additive manufacturing”. In: *Modelling and Simulation in Materials Science and Engineering* 28.065003 (2020). DOI: 10.1088/1361-651X/ab9734.

[23] “Evolution of grain structure during laser additive manufacturing. Simulation by a cellular automata method”. In: *Materials & Design* 106 (2016), pp. 321–329. ISSN: 0264-1275. DOI: https://doi.org/10.1016/j.matdes.2016.05.125. URL: https://www.sciencedirect.com/science/article/pii/S0264127516307481.

[24] Wenda Tan and Xuxiao Li. “Numerical Modeling of Grain Growth in Laser Engineered Net Shaping (LENS) of AISI 316 Stainless Steel”. In: June 2017, V002T01A004. DOI: 10.1115/MSEC2017-2873.

[25] Xuxiao Li and Wenda Tan. “Numerical investigation of effects of nucleation mechanisms on grain structure in metal additive manufacturing”. In: *Computational Materials Science* 153 (2018), pp. 159–169. DOI: 10.1016/j.commatsci.2018.06.019.

[26] Carl Herriott et al. “A multi-scale, multi-physics modeling framework to predict spatial variation of properties in additive-manufactured metals”. In: *Modelling and Simulation in Materials Science and Engineering* 27.2 (Jan. 2019), p. 025009. DOI: 10.1088/1361-651X/aaf753.

[27] Ch.-A Gandin and M Rappaz. “A 3D Cellular Automaton algorithm for the prediction of dendritic grain growth”. In: *Acta Materialia* 45.5 (1997), pp. 2187–2195. DOI: https://doi.org/10.1016/S1359-6454(96)00303-5. URL: https://www.sciencedirect.com/science/article/pii/S1359645496003035.

[28] M.R. Stoudt et al. “Location-Specific Microstructure Characterization Within IN625 Additive Manufacturing Benchmark Test Artifacts”. In: *Integrating Materials and Manufacturing Innovation* 9 (2020), pp. 54–69. DOI: https://doi.org/10.1007/s40192-020-00172-6.

[29] Luke Scime, Alka Singh, and Vincent Paquit. “A scalable digital platform for the use of digital twins in additive manufacturing”. In: *Manufacturing Letters* 31 (2022), pp. 28–32. ISSN: 2213-8463. DOI: https://doi.org/10.1016/j.mfglet.2021.05.007. URL: https://www.sciencedirect.com/science/article/pii/S2213846321000365.

[30] L. Scime et al. *Peregrine: Advanced Data Analytics and Quality Assurance for Powder Bed Additive Manufacturing*. Computer Program. URL: https://www.ornl.gov/technology/90000077.

[31] Luke Scime et al. “Layer-wise anomaly detection and classification for powder bed additive manufacturing processes: A machine-agnostic algorithm for real-time pixel-wise semantic segmentation”. In: *Additive Manufacturing* 36 (2020), p. 101453. ISSN: 2214-8604. DOI: https://doi.org/10.1016/j.addma.2020.101453. URL: https://www.sciencedirect.com/science/article/pii/S2214860420308253.

[32] Gerald L. Knapp et al. “Leveraging the digital thread for physics-based prediction of microstructure heterogeneity in additively manufactured parts”. In: *Additive Manufacturing* 78 (2023), p. 103861. ISSN: 2214-8604. DOI: https://doi.org/10.1016/j.addma.2023.103861. URL: https://www.sciencedirect.com/science/article/pii/S2214860423004748.

[33] Matthew Rolchigo et al. “Sparse thermal data for cellular automata modeling of grain structure in additive manufacturing”. In: *Modelling and Simulation in Materials Science and Engineering* 28.6 (2020), p. 065003. ISSN: 0965-0393. DOI: 10.1088/1361-651X/ab9734. URL: https://dx.doi.org/10.1088/1361-651X/ab9734.